Characteristics of the plasma distribution in Mercury's equatorial magnetosphere derived from MESSENGER Magnetometer observations

Haje Korth,[1] Brian J. Anderson,[1] Catherine L. Johnson,[2,3] Reka M. Winslow,[3] James A. Slavin,[4] Michael E. Purucker,[5] Sean C. Solomon,[6,7] and Ralph L. McNutt Jr.[1]

Received 26 June 2012; revised 3 October 2012; accepted 17 October 2012; published 22 December 2012.

[1] Localized reductions in the magnetic field associated with plasma pressure in Mercury's magnetospheric cusp and nightside plasma sheet have been routinely observed by the Magnetometer on the MErcury Surface, Space ENvironment, GEochemistry and Ranging (MESSENGER) spacecraft. We present a statistical analysis of near-equatorial magnetic depressions to derive the structure of Mercury's plasma sheet pressure. Because the plasma pressure in the magnetosphere correlates with solar wind density, the pressures were normalized to a Mercury heliocentric distance of 0.39 AU. A model magnetic field was used to map observations obtained on the ascending and descending orbit nodes to the magnetic equator and revealed the presence of plasma in a toroidal section extending on the nightside from dusk to dawn. Mapping the data to invariant magnetic latitude shows that the pressure is symmetric about the magnetic equator. The average pressure normalized for heliocentric distance is 1.45 nPa and exhibits a weak, 0.05 nPa/h, dusk-to-dawn gradient with local time. The plasma sheet pressure can vary between successive orbits by an order of magnitude. Unlike the predictions of some global simulations of Mercury's magnetosphere, the plasma enhancements do not form a closed distribution around the planet. This difference may arise from the idealized solar wind and interplanetary magnetic field conditions used in the simulations, which maximize the size and stability of the magnetosphere, thus promoting the formation of drift paths that close around the planet. For typical plasma sheet energies, 5 keV, the first adiabatic invariant for protons fails to be conserved even within 500 km altitude at midnight, implying that stochastic processes must be considered in plasma sheet transport.

Citation: Korth, H., B. J. Anderson, C. L. Johnson, R. M. Winslow, J. A. Slavin, M. E. Purucker, S. C. Solomon, and R. L. McNutt Jr. (2012), Characteristics of the plasma distribution in Mercury's equatorial magnetosphere derived from MESSENGER Magnetometer observations, *J. Geophys. Res.*, *117*, A00M07, doi:10.1029/2012JA018052.

1. Introduction

[2] The convection of magnetic flux in planetary magnetospheres is driven by the solar wind electric field, which is tapped during reconnection of interplanetary and planetary magnetic field lines at the magnetopause [*Dungey*, 1961]. For a southward directed planetary moment, subsolar reconnection is strongest for southward interplanetary magnetic field (IMF), and, in the magnetotail, open magnetic field lines carry solar wind and planetary plasma naturally toward the magnetic equator and then planetward in the presence of the cross-tail electric field, **E**, and the magnetospheric magnetic field, **B**, via the $\mathbf{E} \times \mathbf{B}$ drift [e.g., *Hughes*, 1996]. The resulting concentration of plasma near the magnetic equatorial plane is termed the plasma sheet. In this paper, the plasma sheet properties in Mercury's magnetosphere are examined from orbital Magnetometer (MAG) [*Anderson et al.*, 2007] data obtained by the MErcury Surface, Space ENvironment, GEochemistry, and Ranging (MESSENGER) spacecraft [*Solomon et al.*, 2001].

[3] On 18 March 2011, the MESSENGER spacecraft was inserted into a near-polar orbit about Mercury with an initial periapsis altitude of 200 km (0.08 R_M, where R_M = 2440 km is Mercury's radius), an inclination of 82.5°, an apoapsis altitude of 15,300 km (6.27 R_M), and a period of 12 h. Upon

[1]The Johns Hopkins University Applied Physics Laboratory, Laurel, Maryland, USA.
[2]Planetary Science Institute, Tucson, Arizona, USA.
[3]Department of Earth, Ocean, and Atmospheric Sciences, University of British Columbia, Vancouver, British Columbia, Canada.
[4]Department of Atmospheric, Oceanic and Space Sciences, University of Michigan, Ann Arbor, Michigan, USA.
[5]Solar System Exploration Division, NASA Goddard Space Flight Center, Greenbelt, Maryland, USA.
[6]Department of Terrestrial Magnetism, Carnegie Institution of Washington, Washington, D.C., USA.
[7]Lamont-Doherty Earth Observatory, Columbia University, Palisades, New York, USA.

Corresponding author: H. Korth, The Johns Hopkins University Applied Physics Laboratory, 11100 Johns Hopkins Rd., Laurel, MD 20723, USA. (haje.korth@jhuapl.edu)

0148-0227/12/2012JA018052

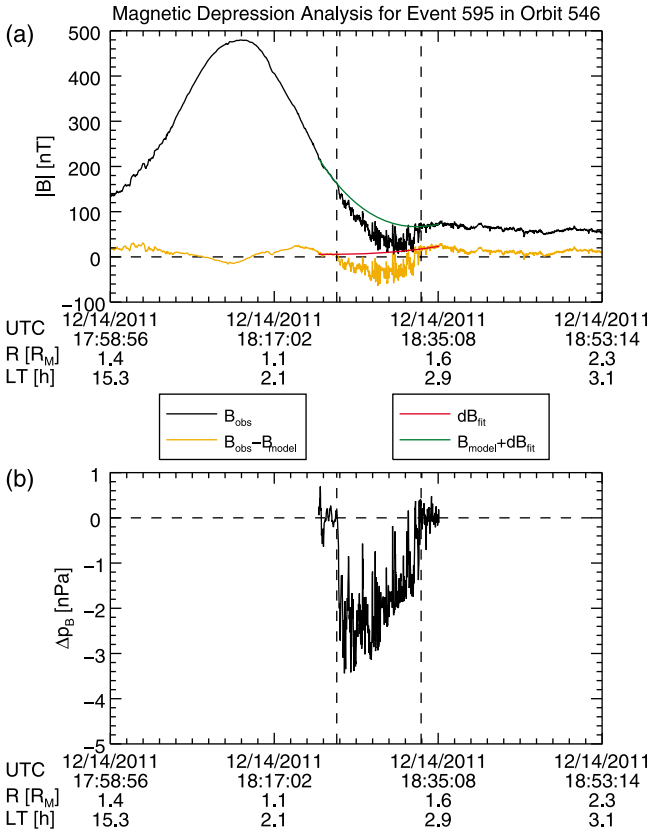

Figure 1. Magnetic depression event observed on 14 December 2011. (a) Time series of the magnitudes of the observed magnetic field (black), model residual magnetic field (orange), baseline magnetic field fit (red), and model magnetic field corrected with the baseline fit (green). (b) Time series of the magnetic pressure deficit. In both panels, the boundaries of the depression event intervals are marked by vertical dashed lines. R is the distance from the planet center, and LT is the local time.

resumption of MAG observations on 23 March 2011, the magnetic field showed systematic depressions to values below those predicted by a planetary dipole field corrected for magnetic fields associated with external current systems [*Korth et al.*, 2011; *Winslow et al.*, 2012]. The magnetic depressions were attributed to local deficits in the magnetic pressure resulting from the presence of enhanced plasma pressures. Regions of enhanced plasma pressure along the MESSENGER orbit are the northern magnetic cusp [*Winslow et al.*, 2012] and the plasma sheet [*Korth et al.*, 2011]. Consequently, the magnetic depressions were predominantly observed on the dayside at high latitude and near the equator on the nightside, and their distribution in magnetic latitude and local time was in good agreement with the enhancement of proton flux in the energy range from 50 eV/q to 20 keV/q observed by the Fast Imaging Plasma Spectrometer (FIPS), one of two sensors on the Energetic Particle and Plasma Spectrometer (EPPS) [*Andrews et al.*, 2007]. The distributions of both the magnetic pressure deficits and the proton fluxes showed gradients directed from dusk to dawn within the plasma sheet, indicating that the plasma pressure at dawn is systematically higher than at dusk. Although counterintuitive from the perspective of drifting ions because these particles drift predominantly duskward in magnetospheres with a southward planetary moment, *Korth et al.* [2011] proposed ion pileup at the dawnside stagnation point to explain the dusk-to-dawn gradient.

[4] We have expanded on the initial work by *Korth et al.* [2011] in several respects. First, we have extended the data set from 4 to 10 months to improve the statistical accuracy of the results and include ascending orbit node observations. Second, we have corrected for the effects of Mercury heliocentric distance and reexamined the local time pressure gradients in the plasma sheet. Mercury's orbit around the Sun is substantially eccentric, with perihelion and aphelion distances of 0.31 and 0.47 AU, respectively. Because the average solar wind conditions vary with heliocentric distance and because the local times sampled by MESSENGER correlate with Mercury true anomaly, the heliocentric distance of the observations must be taken into consideration. Third, since the work by *Korth et al.* [2011], observations of magnetic depressions have been obtained at larger planetocentric distances on the ascending node of the orbit. We have compared the distribution of these observations with those obtained closer to the planet on the descending orbit node. Finally, we have mapped the plasma pressure enhancements along magnetic field lines of force both to low altitudes and to the equatorial plane to test their organization by the magnetospheric magnetic field.

[5] The paper is organized as follows. The identification of the magnetic pressure deficit intervals and normalization with respect to heliocentric distance are described in sections 2 and 3, respectively. The observed plasma sheet structure, including symmetry with respect to the magnetic equator, azimuthal and radial pressure gradients, and equatorial distribution, is described in section 4. The statistical distributions are discussed in section 5 and summarized in section 6.

2. Plasma Pressure Derivation

[6] Following instrument commissioning on 23 March 2011, MAG has operated nearly continuously and measured the vector magnetic field at rates of 20 or 2 samples per second, dependent on location along the orbit and available downlink rates. In this study, we use 1 s averages of these data. Figure 1a shows the magnetic field magnitude B (black line) for a typical orbit with the ascending and descending nodes on the dayside and nightside, respectively. The dominant contribution to B is the planet's intrinsic magnetic field, represented by a spin-axis-aligned, southward directed dipole of moment 190 nT R_M^3, and a 479 km northward offset along the spin axis [*Anderson et al.*, 2011, 2012; *Johnson et al.*, 2012]. Superposed on the planetary field, localized depressions in the magnetic field, such as may be seen between the dashed lines in Figure 1, are encountered on most orbits. *Korth et al.* [2011] attributed these depressions to reduced magnetic pressure, $p_B = \frac{B^2}{2\mu_0}$, in the presence of enhanced plasma populations, where μ_0 is the magnetic permeability of free space. *Korth et al.* [2011] computed the plasma pressure enhancement, $\Delta p_{\mathrm{Plasma}}$, under the assumption of total pressure balance:

$$\Delta p_{\mathrm{Plasma}} = -\Delta p_B = \frac{(B_m + \Delta B_m)^2 - B^2}{2\mu_0}. \quad (1)$$

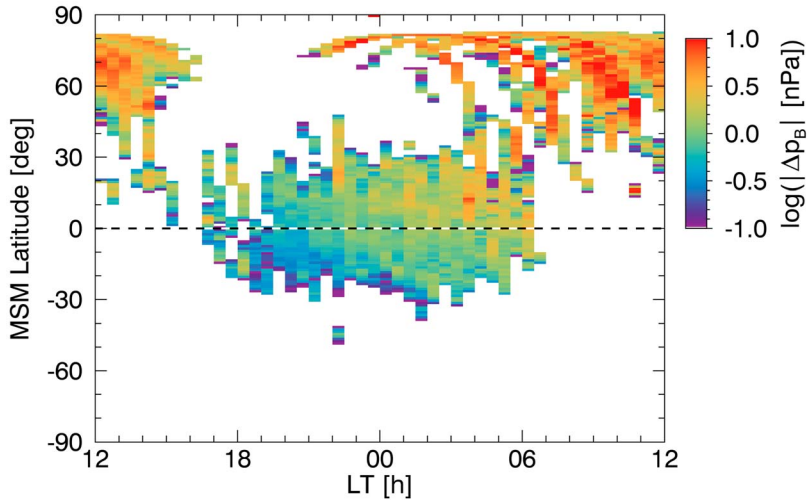

Figure 2. Distribution of the mean magnetic pressure deficits by MSM latitude and local time observed on the descending nodes of the MESSENGER orbit.

In equation (1), $B_m + \Delta B_m$ is the magnetic field of the unperturbed baseline (Figure 1, green line), given by the sum of a static model magnetic field for the internal dipole [*Anderson et al.*, 2011; *Johnson et al.*, 2012] and external current systems [*Alexeev et al.*, 2008, 2010], B_m, and a correction field (red line), ΔB_m, obtained from a third-order polynomial fit (red line) of the magnetic field residual (orange line) up to 2 min on either side of the depression interval. The Δp_B profile for this event is shown in the bottom panel of Figure 1 and typically reaches magnitudes up to 3 nPa.

[7] For statistical analyses of the magnetic depressions we have expanded the database of *Korth et al.* [2011] to include observations from 23 March 2011 to 12 February 2012, spanning four Mercury years and corresponding to four complete local time passes of the MESSENGER spacecraft orbit. The total number of events identified in this interval is 704, more than twice the number available for the previous study. The observations were mapped in Mercury solar magnetospheric (MSM) local time and latitude in 0.5 h and 1°-wide bins, respectively, to yield a representation of the plasma pressure distribution along the MESSENGER orbit. MSM coordinates are centered on the planetary dipole and correspond to Mercury solar orbital (MSO) coordinates displaced 479 km to the north. In both coordinate systems $+X$ is toward the Sun, $+Y$ is duskward, and $+Z$ is northward. We initially considered only those observations obtained on the descending node of the orbit, where the spacecraft crossed the magnetic equator at a mean distance of 3465 km. The features in the resulting distribution, shown in Figure 2, are consistent with those of *Korth et al.* [2011] on the nightside, where enhancements in the plasma pressure are observed in the equatorial region, and additional features are seen in the vicinity of the northern magnetospheric cusp. As shown by *Korth et al.* [2011], the nightside equatorial distribution exhibits a gradient directed from dusk to dawn. In latitude, the magnetic pressure deficits are not centered at 0° magnetic latitude but appear offset to the north. As discussed in section 4, this offset is due to a planetward gradient in the pressure combined with the increase in altitude with decreasing latitude. Finally, several curved tracks are identified at northern high latitudes, each corresponding to an individual orbit evidencing periods of extreme solar wind forcing. The pressure distribution in Figure 2 supersedes that of *Korth et al.* [2011] and is the basis for the detailed analyses below.

3. Normalization of Solar Wind Environment

[8] Mercury's orbit around the Sun is eccentric, so the average gradients in solar wind density and IMF with heliocentric distance will lead to systematic modulation of the planet's solar wind environment over a Mercury year. At Earth, the density in the magnetosphere is well correlated with that in the solar wind, n_{sw} [*Borovsky et al.*, 1998], and changes in n_{sw} likely correlate with plasma pressure variations in Mercury's magnetosphere as well. The variability in n_{sw} with Mercury's heliocentric distance, r_s, is given by the continuity equation, $n_{sw} v_{sw} r_s^2 = \text{const.}$, where v_{sw} is the solar wind speed. Although v_{sw} does have a radial dependence, its increase is rapid close to the Sun, but it approaches nearly constant values beyond a heliocentric distance of about 10 solar radii [*Hundhausen*, 1996]. From the *Parker* [1958] fluid model, *Korth et al.* [2004] approximated the solar wind flow speed at Mercury's orbit with a second-order polynomial, $u_m = 11.06 + 201.04\ r_s - 140.11\ r_s^2$, which yields a variability of about 10% over a Mercury year. Disregarding the small variations in solar wind speed, the solar wind density is approximately proportional to $\frac{1}{r_s^2}$ and at Mercury's orbit is expected to vary by a factor $\left(\frac{0.47}{0.31}\right)^2 \approx 2.3$ over a Mercury year.

[9] Accounting for the variability in solar wind density in the statistical analysis of the plasma pressure inside the magnetosphere is important because the MESSENGER orbit is fixed in inertial space so that the local time sampling is phase locked with respect to heliocentric distance. Figure 3 shows the distribution of the heliocentric distance at which the events in Figure 2 were observed in magnetic local time and latitude. From Figure 3 it is evident that the dusk equatorial region is systematically sampled at larger heliocentric distance than the dawn region. To account for this systematic variation in the solar wind environment, we

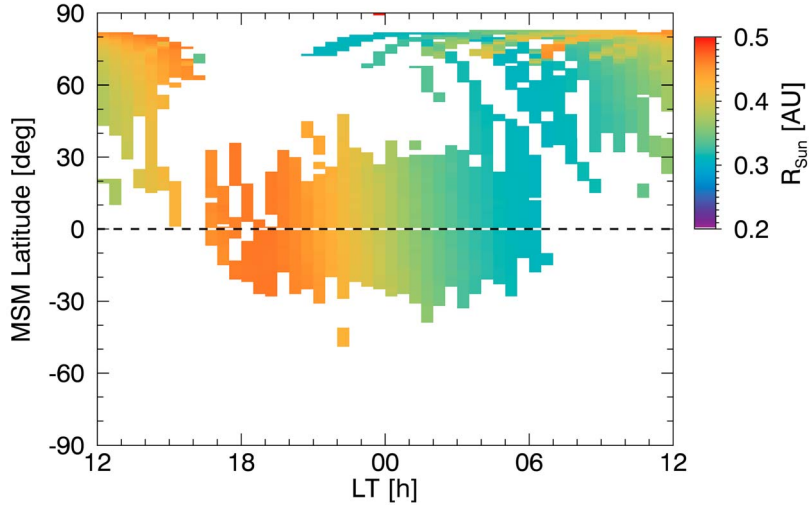

Figure 3. Distribution of the mean heliocentric distance for the p_B observations in Figure 2 shown in the same format.

normalize the pressure distribution in Figure 2 to a uniform distance of 0.39 AU with the scale factor $\left(\frac{r_s}{0.39}\right)^2$. The normalized Δp_B distribution, shown in Figure 4, appears, to first order, uniform across the plasma sheet with typical plasma pressure enhancements in the 1–3 nPa range. This uniformity implies that any pileup effect is much weaker than suggested by *Korth et al.* [2011].

[10] On the ascending node, the MESSENGER spacecraft crosses the magnetic equator at an average planetocentric distance of 6268 km, about 2800 km tailward of the descending node, thus allowing us to extend the previous analysis of *Korth et al.* [2011] to higher altitudes. The distribution of the magnetic pressure deficit for the distant tail crossings normalized with respect to heliocentric distance is shown in Figure 5 in the same format as in Figure 4. Similar to the descending node observations, the pressure distribution obtained on the ascending node shows enhancements in the nightside plasma sheet and the cusp and is skewed toward northern latitudes in MSM coordinates. Comparing Figures 4 and 5 shows that the magnitude of the pressure enhancements associated with the plasma sheet is lower at high altitudes than at low altitudes. At low altitudes, the average pressure increase evaluated over MSM local time (LT) and latitude ranges from 1800 LT to 0600 LT and 30°S to 30°N, respectively, is 1.7 nPa. In contrast, at high altitudes the average pressure increase is about a factor of 2 lower (0.8 nPa). To separate the radial gradient from the variation in latitude, we consider the pressures mapped to invariant latitude.

4. Plasma Sheet Structure

4.1. Symmetry About Magnetic Equator

[11] To map the pressure distribution to invariant magnetic coordinates, the pressure observations must be related

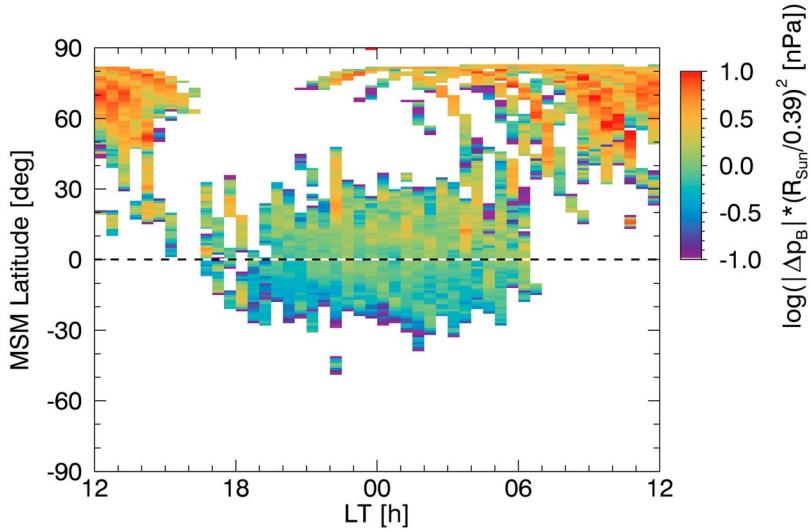

Figure 4. Distribution of the mean magnetic pressure deficits observed on the descending nodes normalized by heliocentric distance in the same format as Figure 2.

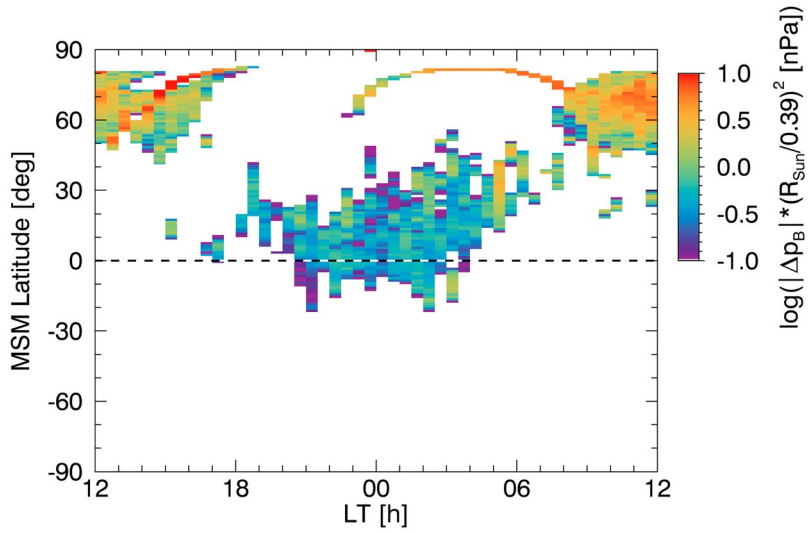

Figure 5. Distribution of the mean magnetic pressure deficits observed on the ascending nodes normalized by heliocentric distance in the same format as Figure 2.

to the geometry of the magnetic field lines on which they were made. This step is accomplished by tracing each observing location along its respective field line to the nearest intersection with a sphere of radius R_M centered on the offset dipole moment; the latitude of the foot point on this sphere is the invariant latitude, Λ. For this calculation we used the *Alexeev et al.* [2008, 2010] magnetic field model parameterized with a subsolar magnetopause standoff distance of 1.45 R_M, a magnetopause flaring factor of 1, a tail current sheet having a thickness of 0.5 R_M and an inner edge located at 1.32 R_M radial distance from the planet center, and a lobe magnetic field of 145 nT [cf. *Anderson et al.*, 2011]. By Liouville's theorem, plasma pressure is invariant along the field line. Figure 6 shows the distribution of the magnetic pressure deficit in Λ and local time of the field line foot point for the complete set of events, i.e., it includes both the ascending and the descending node observations. The observations were normalized with respect to heliocentric distance as discussed in section 3. The pressure events observed in the plasma sheet map to two approximately 30°-wide bands in the midlatitude northern and southern hemisphere separated by a gap in the equatorial region. The gap (delimited by black lines in Figure 6) is located on field lines that are not intersected by the MESSENGER orbit. The mapped plasma sheet pressure enhancements in the northern hemisphere appear further separated into equatorward and poleward bands, corresponding to mapping of the low- and high-altitude observations, respectively. The gap in between these regions is an artifact resulting from limitations in the detection of the magnetic depressions. At northern latitudes, the dipole field sampled by MAG is both large in magnitude and strongly varying along the orbit so that the embedded

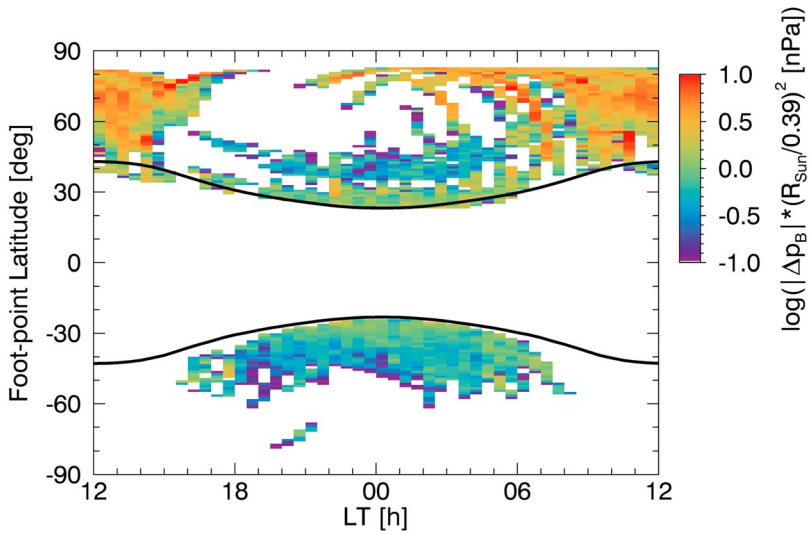

Figure 6. Distribution of the mean magnetic pressure deficits with respect to invariant latitude and local time of the closest field line foot point on a sphere of radius 1 R_M centered on the offset internal field dipole.

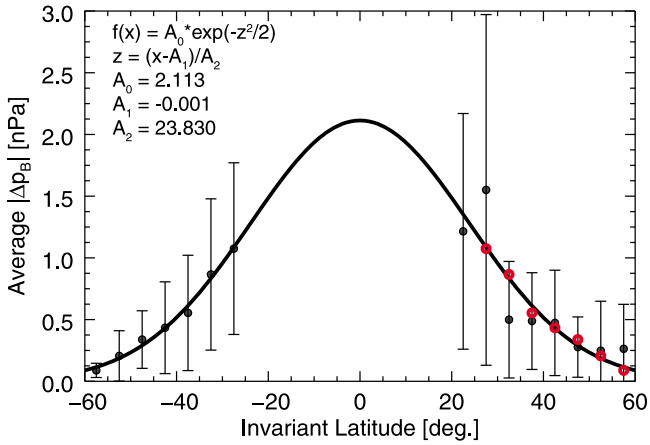

Figure 7. Gaussian fit of the average magnetic pressure deficit within 2 h of local midnight as a function of invariant latitude. The error bars represent the 1σ standard deviations of the magnetic pressure deficits in the respective latitude bin. For comparison, the southern hemisphere data are shown mirrored into the northern hemisphere as red circles. The fit parameters are listed.

magnetic depression signatures are often difficult to discern in this region. In contrast, the magnetic depressions near the equator and in the southern hemisphere are observed within regions of relatively weak background fields varying only slowly along the orbit. Here, the depression intervals are typically unambiguously identified, thus explaining the smooth and continuous latitudinal gradient near and south of the magnetic equator. Comparing the latitudinal extent of the plasma sheet pressure enhancement in the northern and southern hemisphere, the symmetry of the pressure distribution with respect to the magnetic equator is evident.

[12] From a subset of the events observed within ±2 h of local midnight and ±60° latitude, we further examined the degree of symmetry in the pressure distribution with Λ. For this examination, the pressure observations were first sorted into and averaged within 5°-wide bins in Λ. The corresponding profile in Figure 7 shows that the pressure averages (black dots) increase toward the magnetic equator in both hemispheres. For reasons discussed above, the increase is smoother in the southern hemisphere than it is in the northern hemisphere. Mirroring the data points in the southern hemisphere to the north (red circles) shows that the data points in both hemispheres are clustered similarly. A Gaussian fit, $f(x) = p_0 e^{-\frac{z^2}{2}}$, where $z = \frac{\Lambda - \bar{\Lambda}}{\sigma^2}$, of the observations (black dots) yields a maximum pressure increase of $p_0 = 2.1 \pm 0.3$ nPa at a mean invariant latitude $\bar{\Lambda} = 0.0° \pm 1.3°$ and variance $\sigma^2 = 23.8° \pm 2.0°$, demonstrating the high degree of symmetry of the pressure distribution about the magnetic equator near local midnight. Since the magnetospheric plasma is expected to be organized by the magnetic field, the symmetry of the plasma sheet pressure enhancements provides an independent verification of the dipole offset from the geographic equator.

4.2. Azimuthal Pressure Gradient

[13] We next examined the data for azimuthal structure in the plasma sheet pressure. Because the MESSENGER spacecraft traverses the plasma sheet on ascending and descending orbit nodes at different radial distances from the planet, we analyzed the data for two distinct distances in the tail. For this analysis we normalized the magnetic pressure deficits for each event to $r_s = 0.39$ AU as described above and computed the mean Δp_B value for each event. We then restricted the analysis to the plasma sheet by selecting only those observations presumably obtained on closed magnetic field lines, i.e., regions of space within which the model field lines can be traced to intersect the planet at both ends. Furthermore, only events in the nightside local time range from dusk (1800 LT) to dawn (0600 LT) were retained for further analysis. Figure 8 shows the Δp_B averages as a function of mean local time for the descending orbit tracks nearer the planet.

[14] At fixed local times, the data in Figure 8 show a spread over approximately an order of magnitude, implying substantial variability in the plasma pressure from orbit to orbit. The straight line fit (red line) to the data yields Δp_B magnitudes of 1.25 nPa and 1.75 nPa at dusk and dawn, respectively, thus indicating the persistence of a small dusk-to-dawn gradient. However, the slope of 0.05 nPa/h for the best fit is lower than the three standard deviation (3σ) uncertainty in this parameter (0.06 nPa/h), and the correlation coefficient of 0.19 further suggests that the variation in plasma sheet pressures with local time is less significant than its temporal variability. Similar findings were obtained from observations on closed field lines of the ascending node (not shown), for which the fit of the mean pressure enhancement versus local time yields a duskside pressure of 0.73 ± 0.03 nPa, with an increase of 0.04 ± 0.06 nPa/h toward dawn, and a correlation coefficient of 0.07. Thus, there is weak evidence for a persistent organization of the plasma sheet properties from particle drift such as is observed at Earth [*Korth et al.*, 1999; *Friedel et al.*, 2001]. Nonetheless, we conclude that the solar wind density provides the primary forcing for the systematic dusk-to-dawn plasma pressure gradient reported by *Korth et al.* [2011]. Evidence for systematic particle drifts must thus be reexamined using the magnetic pressure deficit estimates normalized by heliocentric distance. The orbit-to-orbit variability in plasma pressure is up to an order of magnitude, and the mechanisms responsible for this dynamics remain to be determined.

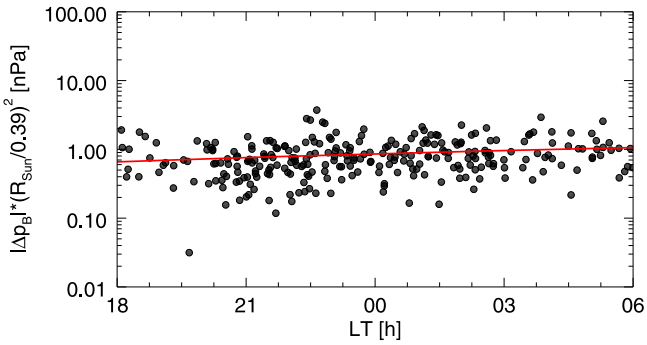

Figure 8. Local time dependence of the mean magnetic pressure deficit for the descending orbit tracks normalized by heliocentric distance. The red line fit to these data has an offset with respect to the origin of 1.45 ± 0.06 nPa and a slope of 0.05 ± 0.02 nPa/h directed from dusk to dawn. The correlation coefficient is 0.19.

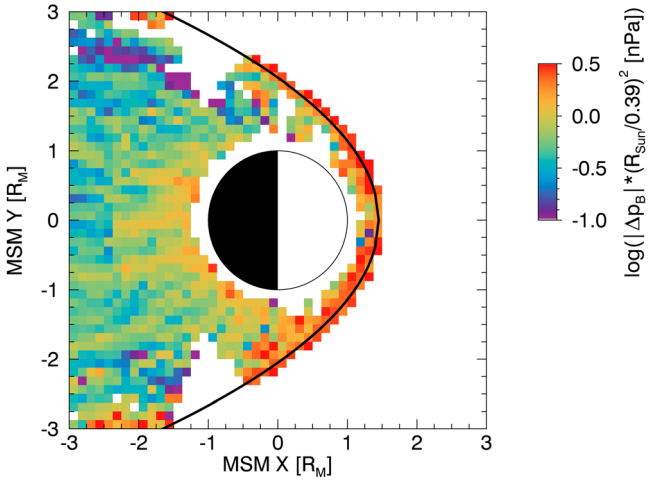

Figure 9. Equatorial distribution of the mean magnetic pressure deficit normalized by heliocentric distance. The Sun is to the right, and the magnetopause of the *Alexeev et al.* [2008, 2010] magnetic field model is represented by the solid black line.

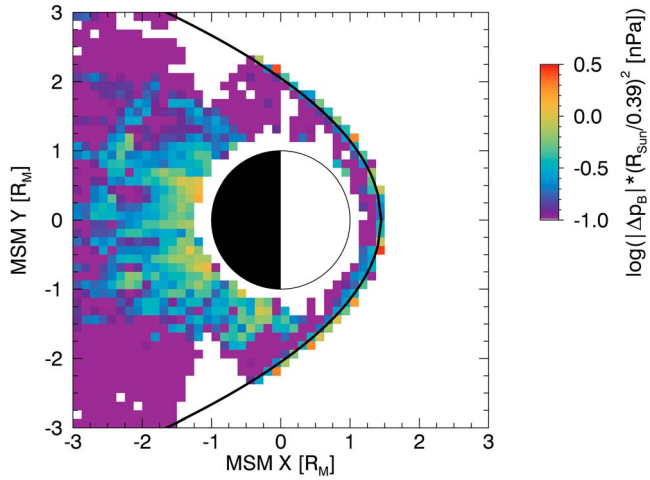

Figure 10. Equatorial distribution of the mean magnetic pressure deficit normalized by heliocentric distance and by the ratio of the number of orbits contributing to the observations in each bin to the total number of orbits whose traced magnetic equator point passed through each bin.

4.3. Equatorial Pressure Distribution

[15] The magnetic field line mapping technique can also be used to determine the equatorial pressure distribution. This step is accomplished by tracing the event locations along field lines to the magnetic equatorial plane and assigning the observed pressure deficit to that location. Here we averaged the equatorially mapped pressure observations in bins of dimensions 0.125 $R_M \times 0.125$ R_M. The statistical distribution derived in this manner is presented in Figure 9, showing the Δp_B values color-coded according to magnitude in the MSM $X - Y$ plane at $Z = 0$. The plasma pressure enhancements are found to be largest near the planet, where they appear approximately uniform in local time, although the pressures appear slightly higher on the dayside. On the nightside, a decrease in the equatorial pressure distribution at larger planetocentric distances is evident. Note that the $\mathbf{E} \times \mathbf{B}$ drift that the protons experience during their bounce motion toward the equatorial plane is not considered in the mapping process. The resulting uncertainty in the mapping is on the order of one grid cell dimension and thus does not affect the identification of large-scale features in the distribution.

[16] To identify regions where plasma pressure enhancements are most prevalent, the distribution of Figure 9 was normalized by the ratio of the number of orbits contributing to the observations in each bin to the total number of orbits for which the traced magnetic equatorial point passed through each bin. The orbit-normalized distribution (Figure 10) shows that the most marked pressure enhancements are most commonly encountered on the nightside at radial distances ranging from the inner boundary of the observations at 0.25 R_M to about 2 R_M. On the dayside, pressures near the model magnetopause are much reduced compared with those in Figure 9, indicating that the magnetopause pressure enhancements in that figure were due to cusp pressure observations from a few events having erroneously been identified as on closed field lines in the model.

[17] The equatorial pressure distributions do not reveal any systematic nightside gradients in the dawn–dusk direction. Rather, there is an inward radial gradient that appears to be comparable across the nightside. This gradient could be due to either acceleration or heating of plasma as it is convected from the tail toward the planet. Embedded in this large-scale feature are near-radial enhancements on the nightside, which reflect orbit tracks of events with particularly large Δp_B. The associated plasma pressure enhancements are directly controlled by solar wind and IMF conditions imposed on the magnetosphere, so these Δp_B observations are most likely associated with extreme solar wind conditions, including those produced by coronal mass ejections and interplanetary shocks. The fact that especially at greater distances from the planet the statistics are influenced by relatively few events with large Δp_B implies that the average characteristics of particle motion, such as the duskward drift of the protons observed at Earth, may be overwhelmed by rapid dynamics in

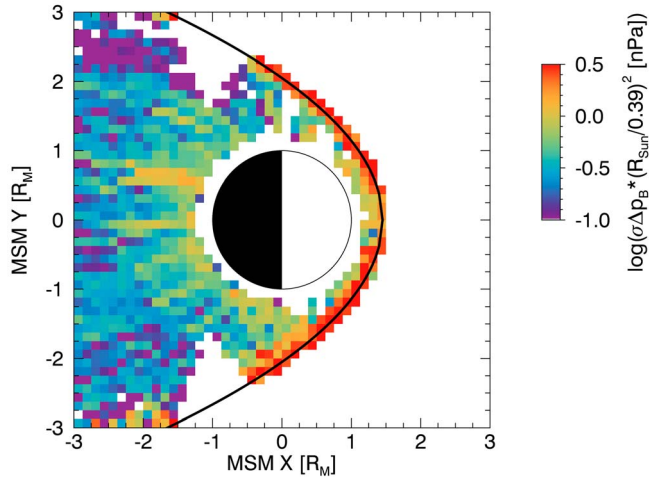

Figure 11. Equatorial distribution of the standard deviations in the magnetic pressure deficit normalized by heliocentric distance.

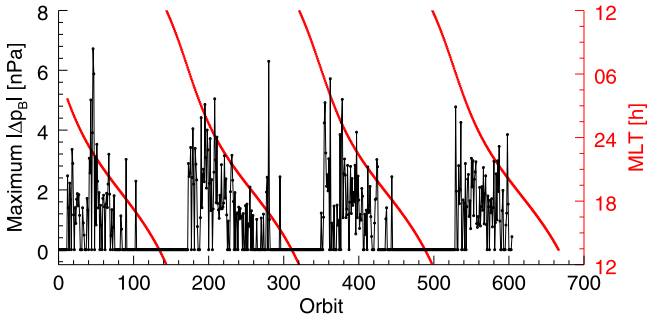

Figure 12. Peak magnetic pressure deficit observed on the descending node as a function of orbit number (black symbols and line). The pressure deficits for orbits with no magnetic depressions identified were set to zero. The magnetic local time (MLT) at the equatorial crossing of the descending node is shown in red.

Mercury's magnetosphere. To quantify the variability of the observed Δp_B, we show in Figure 11 the 1σ standard deviations in the bin averages of the pressure distribution. Comparison with Figure 9 shows that the standard deviations, $\sigma_{\Delta p_B}$, and the bin averages are similar in magnitude, and the average ratio $\frac{\sigma_{\Delta p_B}}{\Delta_{p_B}}$ computes to 0.7. The variance in the statistical distribution of the plasma pressure is significantly larger than the dawn–dusk pressure ratio of ~2 observed in the terrestrial magnetosphere [*Korth et al.*, 1999] and results from large orbit-to-orbit variability. Figure 12 shows the peak magnetic pressure deficit observed on the descending node of the orbit as a function of orbit number. The pressure for orbits during which no magnetic depressions were observed was set to zero. The difference in the equatorial pressure typically varies by several nPa between successive orbits. Also shown in Figure 12 is the magnetic local time at the equatorial crossing on the descending node. Consistent with the statistical distributions above, depressions near the equator are predominantly found on the nightside, and for most nightside transitions of the orbit a pressure peak is observed near local midnight. We conclude that the statistics of the MAG data set to date are insufficient to allow the identification of a systematic drift pattern in Mercury's magnetosphere.

5. Discussion

[18] The key features of Mercury's plasma sheet identified from MESSENGER MAG data in this study are as follows: the plasma sheet is localized in a toroidal section (see Figure 10) that extends on the nightside from dusk to dawn; it is centered at the magnetic equator near local midnight; it exhibits an inward radial pressure gradient but no prominent gradient in local time; the pressure appears to scale with the solar wind density; and the pressure varies by more than an order of magnitude from orbit to orbit, that is, on time scales shorter than 12 h. We next consider what these features may imply for plasma transport.

[19] If plasma convection proceeds at Mercury as it does at Earth, this plasma population near Mercury could arise from plasma convected from the tail toward the planet to the inner magnetosphere by the $\mathbf{E} \times \mathbf{B}$ drift and subsequent distribution of the charged particles around the planet by the gradient and curvature drifts. In this scenario, an inward pressure gradient forms as both the density and temperature of the plasma increase during the transport to higher magnetic field strengths near the planet. The density increase results from particles being confined in progressively smaller magnetic flux tube volumes during transport closer to the planet, while, simultaneously, the ion temperature increases due to acceleration by the dawn-to-dusk electric field [*Korth et al.*, 2011]. At Earth, the plasma sheet pressure at fixed radial distance does not vary greatly from dawn to dusk [*Wang et al.*, 2006], but closer to Earth, where the gradient curvature drift is stronger, the energies and densities of the drifting ion populations vary systematically with local time [*Korth et al.*, 1999].

[20] After normalizing the magnetic pressure deficits for solar wind density variation with heliocentric distance, we do not find evidence for a strong dusk-to-dawn gradient in the plasma pressure distribution previously identified by *Korth et al.* [2011] and attributed to an accumulation of charged ions at their dawnside stagnation point. From the perspective of particle drifts, the direction of the gradient presented in the above work was unexpected because in magnetospheres with a southward planetary moment, the gradient and curvature drifts of hot ions are in the duskward direction on the nightside. Since hot ions constitute the dominant source for the plasma pressure, one would expect a pressure increase toward dusk corresponding to a gradient in direction opposite to that found by *Korth et al.* [2011], i.e., dawn to dusk. The absence of a significant pressure gradient with local time in the nightside plasma at Mercury may indicate that the plasma sheet proper extends very close to the planet so that conventional adiabatic drift processes responsible for local time gradients at Earth are not dominant. It is of course possible that some balance of density pileup, heating, or losses could combine to reduce the local time structure.

[21] The foregoing discussion of plasma convection is predicated on the assumption that particles follow guiding center drift motions. To test this assumption, we examine the change in the magnetic moment, μ, experienced during a particle's transit through the minimum curvature region [*Birmingham*, 1984; *Anderson et al.*, 1997]:

$$\frac{\Delta\mu}{\mu} \cong -\delta_B \cos\Psi_{\mathrm{eq}}, \tag{2}$$

where ψ_{eq} is the equatorial gyrophase and δ_B is a function of $\varepsilon = 1/\kappa^2$, where κ is the kappa parameter [*Büchner and Zelenyi*, 1989]. Given the particle's equatorial pitch angle, α_{eq}, δ_B is given by

$$\delta_B = \frac{\pi}{2^{\frac{1}{4}}\,\Gamma\left(\frac{9}{8}\right)} \frac{1}{\varepsilon^{\frac{1}{8}} \sin\alpha_{\mathrm{eq}}} \exp\left[-\frac{F\left(\sin\alpha_{\mathrm{eq}}\right)}{\varepsilon}\right], \tag{3}$$

$$F\left(\sin\alpha_{\mathrm{eq}}\right) \approx \frac{2}{3} + \frac{3\pi}{32}\sin^2\alpha_{\mathrm{eq}} + \frac{1}{15}\sin^4\alpha_{\mathrm{eq}}. \tag{4}$$

Anderson et al. [1997] showed that δ_B is better correlated with $\Delta\mu/\mu$ than ε or κ alone and that for $\delta_B > 0.01$ and repeated equatorial crossings, the dependence of the net $\Delta\mu$ on the gyrophase is so sensitive that μ scattering is chaotic and particle motion becomes nonadiabatic. Figure 13 shows

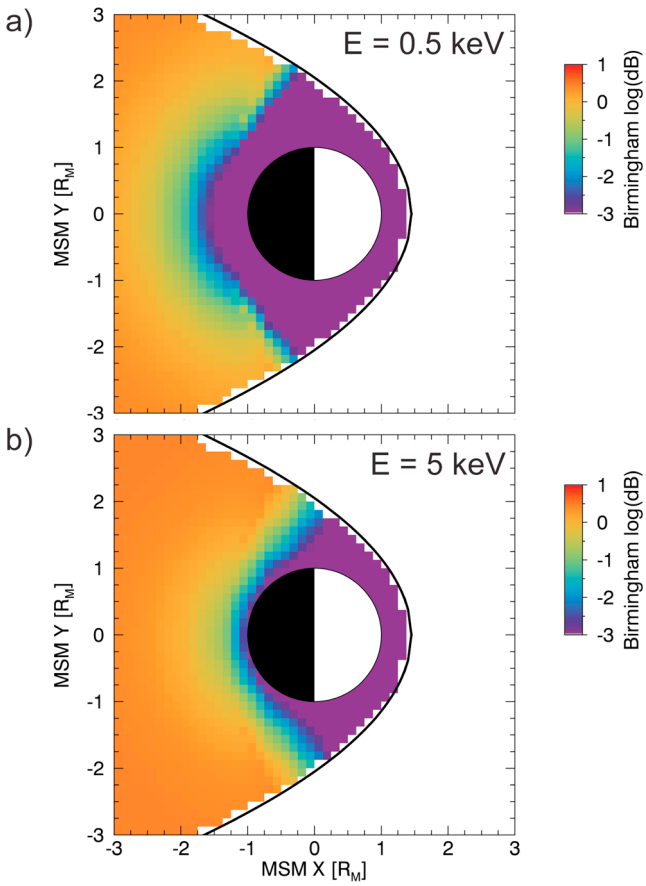

Figure 13. Distribution of the Birmingham δ_B parameter in the magnetic equatorial plane for protons of (a) 0.5 keV and (b) 5 keV energy.

the distribution of the δ_B parameter in the magnetic equatorial plane for the magnetospheric field model that best fits the MESSENGER observations and that has been used in this study for protons having a pitch angle of $\alpha_{eq} = 45°$ and energies of 0.5 keV (Figure 13a) and 5 keV (Figure 13b). The higher energy is the characteristic energy of protons observed by MESSENGER in Mercury's plasma sheet [*Zurbuchen et al.*, 2011]. For both energies, we find $\delta_B >$ 0.01 over nearly the entire nightside magnetotail, indicating that particle motion is commonly nonadiabatic in much of Mercury's plasma sheet. This behavior leads to chaotic scattering into the loss cone and meandering particle motion in this region [*Delcourt et al.*, 2003], so that the guiding center drift approximation of *Korth et al.* [2011] is not applicable in most of Mercury's magnetosphere. Particle drift motions still occur, but they are accompanied by pitch angle scattering and meandering orbits. Only near the planetary surface may a region allowing for adiabatic particle motion exist for protons with sub-keV energies. The unstructured nature of the plasma sheet is thus not surprising under these conditions, and rapidly fluctuating solar wind conditions imposed on the magnetosphere are likely to decrease further the organization in plasma sheet structure.

[22] We do find that there may be a small dawn–dusk asymmetry in the pressure distribution (see Figure 10). A dawnside pressure enhancement may be consistent with sources at the planet [*Yagi et al.*, 2010] and the low-latitude boundary layer [*Nagano*, 1979; *Sundberg et al.*, 2010]. In addition, hybrid simulations of Mercury's magnetosphere show that the inner magnetosphere can be populated by protons undergoing gradient curvature drift westward from the dawn side after entering at the cusp [*Trávníček et al.*, 2007, 2009, 2010; *Schriver et al.*, 2011]. A dawnside source near the planet could account for the absence of a strong dawn–dusk gradient, since the tail electric field is not involved in accelerating the particles, as well as for the inward gradient, since the source is localized to field lines close to the planet.

[23] However, loss processes are expected to be substantial and should be considered in any quantitative comparison with the observations. During the drift around the planet from the nightside to the dayside, the plasma population is depleted through at least three processes: nonadiabatic motion, leading to pitch angle scattering into the large (~30° angle) loss cone; resonant wave–particle interactions that also scatter particles into the loss cone [*Boardsen et al.*, 2009; *Trávníček et al.*, 2010; *Schriver et al.*, 2011]; and charge exchange with exospheric neutral atoms, although this last process has only a small effect at Mercury [*Milillo et al.*, 2005; *Mura et al.*, 2006]. For heavy ion species such as Na^+, losses via collision with the planetary surface and magnetopause boundary during their gyration about the guiding magnetic field line are also substantial [*Delcourt et al.*, 2003; *Yagi et al.*, 2010], but these species were found to contribute only a small fraction, ~15%, to the total pressure in the plasma sheet [*Zurbuchen et al.*, 2011]. In consequence, the ion pressures diminish during transport. We find that the plasma pressures are low westward of the dusk terminator; the magnetic field depressions there are not distinguishable from the natural fluctuations in the magnetic field data (see Figure 4). Presumably, however, the losses occur throughout transport westward across the tail, and yet we find only a weak dusk-to-dawn pressure gradient. It remains to be seen how the transport and loss might combine to yield the observed low systematic variation in pressure with local time.

[24] That the inner-magnetospheric plasma population extends only around the nightside is in contrast to inferences from several magnetohydrodynamic [*Benna et al.*, 2010] and kinetic hybrid simulations [*Trávníček et al.*, 2007, 2009, 2010; *Schriver et al.*, 2011], which show a belt of quasi-trapped particles encircling the planet. To distinguish the simulated plasma belt from a truly trapped population, such as the ring current in the terrestrial magnetosphere, *Schriver et al.* [2011] introduced the term "quasi-trapped" because only 10% of the particles complete the drift around the planet whereas the remaining 90% are lost through precipitation. A trapped population is thus barely maintained in the simulation and should not be a prominent feature. Moreover, stable external conditions and correspondingly stable magnetospheric configuration in the simulation may not accurately represent the natural system. The boundary conditions for the simulation discussed by *Schriver et al.* [2011] include a planetary magnetic moment of magnitude 25% larger than that determined recently (but consistent with the best estimate then available), a constant northward IMF, and relatively low solar wind density and speed. The imposed solar wind parameters correspond to stable, magnetically quiet conditions at Mercury's 0.47 AU aphelion distance. The size of Mercury's magnetosphere and the subsolar magnetopause

standoff distance are maximized by each of these assumptions and represent the most favorable conditions for allowing particles to drift around the planet on the dayside. Modifying the simulations to use the most recent determination of the planetary moment, increasing solar wind density and velocity and thus the ram pressure, and/or introducing variable IMF, will likely temporarily interrupt the dayside closed drift paths. Kinetic hybrid simulations of MESSENGER's second Mercury flyby [*Trávníček et al.*, 2010] showed the effect of a smaller magnetosphere as a result of a southward oriented IMF, for which the particles of the plasma belt are found to leak out of the magnetosphere near dusk (their Figure 2c). Thus, although it is possible that the MAG observations are not sufficiently sensitive to detect a tenuous plasma population on the dayside, it is likely that the dayside drift path is not generally available.

6. Summary

[25] We analyzed MESSENGER observations of magnetic field depressions at Mercury, i.e., field magnitudes below those predicted for the planetary dipole with external field contributions. The magnetic depressions correspond to enhanced plasma populations that balance the total pressure and cause the observed deficits in the magnetic pressure. The plasma enhancements were observed predominantly in the cusp and in the nightside plasma sheet. Statistical mapping of Mercury's plasma sheet reveals the existence of a plasma enhancement within a toroidal section, which is centered at the magnetic equator near local midnight and extends on the nightside from dusk to dawn. Unlike the predictions of some global simulations of Mercury's magnetosphere, the plasma enhancements do not form a closed distribution around the planet. This difference is most likely due to the adoption in the simulations of idealized solar wind and IMF conditions, which maximize and stabilize the size of the magnetosphere and thus promote the formation of closed drift orbits around the planet. We find a systematic inward radial pressure gradient but no strong local time variation in pressure. This geometry may be consistent with chaotic, nonadiabatic particle motions that are expected to predominate in Mercury's magnetotail to within a few hundred kilometers of the surface, motions that would suppress the development of azimuthal structures resulting from coherent drift motions. Loss due to the scattering of ions by local instabilities and nonadiabatic particle motion into the precipitation loss cone could be substantial. Whether a dawnside source from the low-latitude boundary layer or cusp entry is sufficient to account for the observed pressures in the presence of precipitation losses is not yet known.

[26] **Acknowledgments.** The MESSENGER project is supported by the NASA Discovery Program under contracts NAS5-97271 to The Johns Hopkins University Applied Physics Laboratory and NASW-00002 to the Carnegie Institution of Washington. C.L.J. and M.E.P. are supported by MESSENGER Participating Scientist grants NNX11AB84G and NNH08CC05C. R.M.W. and C.L.J. acknowledge support from the Natural Sciences and Engineering Research Council of Canada.

[27] Masaki Fujimoto thanks the reviewers for their assistance in evaluating this paper.

References

Alexeev, I. I., E. S. Belenkaya, S. Y. Bobrovnikov, J. A. Slavin, and M. Sarantos (2008), Paraboloid model of Mercury's magnetosphere, *J. Geophys. Res.*, *113*, A12210, doi:10.1029/2008JA013368.

Alexeev, I. I., et al. (2010), Mercury's magnetospheric magnetic field after the first two MESSENGER flybys, *Icarus*, *209*, 23–39, doi:10.1016/j.icarus.2010.01.024.

Anderson, B. J., R. B. Decker, N. P. Paschalidis, and T. Sarris (1997), Onset of nonadiabatic particle motion in the near-Earth magnetotail, *J. Geophys. Res.*, *102*, 17,553–17,569, doi:10.1029/97JA00798.

Anderson, B. J., M. H. Acuña, D. A. Lohr, J. Scheifele, A. Raval, H. Korth, and J. A. Slavin (2007), The Magnetometer instrument on MESSENGER, *Space Sci. Rev.*, *131*, 417–450, doi:10.1007/s11214-007-9246-7.

Anderson, B. J., C. L. Johnson, H. Korth, M. E. Purucker, R. M. Winslow, J. A. Slavin, S. C. Solomon, R. L. McNutt Jr., J. M. Raines, and T. H. Zurbuchen (2011), The global magnetic field of Mercury from MESSENGER orbital observations, *Science*, *333*, 1859–1862, doi:10.1126/science.1211001.

Anderson, B. J., C. L. Johnson, H. Korth, R. M. Winslow, M. E. Purucker, J. A. Slavin, S. C. Solomon, and R. L. McNutt Jr. (2012), Low-degree structure in Mercury's planetary magnetic field, *J. Geophys. Res.*, *117*, E00L12, doi:10.1029/2012JE004159.

Andrews, G. B., et al. (2007), The Energetic Particle and Plasma Spectrometer instrument on the MESSENGER spacecraft, *Space Sci. Rev.*, *131*, 523–556, doi:10.1007/s11214-007-9272-5.

Benna, M., et al. (2010), Modeling of the magnetosphere of Mercury at the time of the first MESSENGER flyby, *Icarus*, *209*, 3–10, doi:10.1016/j.icarus.2009.11.036.

Birmingham, T. J. (1984), Pitch angle diffusion in the Jovian magnetodisc, *J. Geophys. Res.*, *89*, 2699–2707, doi:10.1029/JA089iA05p02699.

Boardsen, S. A., B. J. Anderson, M. H. Acuña, J. A. Slavin, H. Korth, and S. C. Solomon (2009), Narrow-band ultra-low-frequency wave observations by MESSENGER during its January 2008 flyby through Mercury's magnetosphere, *Geophys. Res. Lett.*, *36*, L01104, doi:10.1029/2008GL036034.

Borovsky, J. E., M. F. Thomsen, and R. C. Elphic (1998), The driving of the plasma sheet by the solar wind, *J. Geophys. Res.*, *103*, 17,617–617,639.

Büchner, J., and L. M. Zelenyi (1989), Regular and chaotic charged-particle motion in magnetotail-like field reversals: 1. Basic theory of trapped motion, *J. Geophys. Res.*, *94*, 11,821–11,842.

Delcourt, D. C., S. Grimald, F. Leblanc, J. J. Berthelier, A. Millilo, A. Mura, S. Orsini, and T. E. Moore (2003), A quantitative model of the planetary Na^+ contribution to Mercury's magnetosphere, *Ann. Geophys.*, *21*, 1723–1736, doi:10.5194/angeo-21-1723-2003.

Dungey, J. W. (1961), Interplanetary magnetic field and auroral zones, *Phys. Rev. Lett.*, *6*, 47–48, doi:10.1103/PhysRevLett.6.47.

Friedel, R. H. W., H. Korth, M. G. Henderson, M. F. Thomsen, and J. D. Scudder (2001), Plasma sheet access to the inner magnetosphere, *J. Geophys. Res.*, *106*, 5845–5858, doi:10.1029/2000JA003011.

Hughes, W. J. (1996), The magnetopause, magnetotail, and magnetic reconnection, in *Introduction to Space Physics*, edited by M. G. Kivelson and C. T. Russell, pp. 227–287, Cambridge Univ. Press, New York.

Hundhausen, A. J. (1996), The solar wind, in *Introduction to Space Physics*, edited by M. G. Kivelson and C. T. Russell, pp. 91–128, Cambridge Univ. Press, New York.

Johnson, C. L., et al. (2012), MESSENGER observations of Mercury's magnetic field structure, *J. Geophys. Res.*, doi:10.1029/2012JE004217, in press.

Korth, H., M. F. Thomsen, J. E. Borovsky, and D. J. McComas (1999), Plasma sheet access to geosynchronous orbit, *J. Geophys. Res.*, *104*, 25,047–25,061, doi:10.1029/1999JA900292.

Korth, H., B. J. Anderson, M. H. Acuña, J. A. Slavin, N. A. Tsyganenko, S. C. Solomon, and R. L. McNutt Jr. (2004), Determination of the properties of Mercury's magnetic field by the MESSENGER mission, *Planet. Space Sci.*, *52*, 733–746, doi:10.1016/j.pss.2003.12.008.

Korth, H., B. J. Anderson, J. M. Raines, J. A. Slavin, T. H. Zurbuchen, C. L. Johnson, M. E. Purucker, R. M. Winslow, S. C. Solomon, and R. L. McNutt Jr. (2011), Plasma pressure in Mercury's equatorial magnetosphere derived from MESSENGER Magnetometer observations, *Geophys. Res. Lett.*, *38*, L22201, doi:10.1029/2011GL049451.

Milillo, A., et al. (2005), Surface-exosphere-magnetosphere system of Mercury, *Space Sci. Rev.*, *117*, 397–443, doi:10.1007/s11214-005-3593-z.

Mura, A., S. Orsini, A. Milillo, A. M. Di Lellis, and E. De Angelis (2006), Neutral atom imaging at Mercury, *Planet. Space Sci.*, *54*, 144–152, doi:10.1016/j.pss.2005.02.009.

Nagano, H. (1979), Effect of finite ion Larmor radius on the Kelvin-Helmholtz instability of the magnetopause, *Planet. Space Sci.*, *27*, 881–884, doi:10.1016/0032-0633(79)90013-8.

Parker, E. N. (1958), Dynamics of the interplanetary gas and magnetic fields, *Astrophys. J.*, *128*, 664–676, doi:10.1086/146579.

Schriver, D., et al. (2011), Quasi-trapped ion and electron populations at Mercury, *Geophys. Res. Lett.*, *38*, L23103, doi:10.1029/2011GL049629.

Solomon, S. C., et al. (2001), The MESSENGER mission to Mercury: Scientific objectives and implementation, *Planet. Space Sci.*, *49*, 1445–1465, doi:10.1016/S0032-0633(01)00085-X.

Sundberg, T., S. A. Boardsen, J. A. Slavin, L. G. Blomberg, and H. Korth (2010), The Kelvin-Helmholtz instability at Mercury: An assessment, *Planet. Space Sci.*, *58*, 1434–1441, doi:10.1016/j.pss.2010.06.008.

Trávníček, P. M., P. Hellinger, and D. Schriver (2007), Structure of Mercury's magnetosphere for different pressure of the solar wind: Three dimensional hybrid simulations, *Geophys. Res. Lett.*, *34*, L05104, doi:10.1029/2006GL028518.

Trávníček, P. M., P. Hellinger, D. Schriver, D. Herčík, J. A. Slavin, and B. J. Anderson (2009), Kinetic instabilities in Mercury's magnetosphere: Three-dimensional simulation results, *Geophys. Res. Lett.*, *36*, L07104, doi:10.1029/2008GL036630.

Trávníček, P. M., D. Schriver, P. Hellinger, D. Herčík, B. J. Anderson, M. Sarantos, and J. A. Slavin (2010), Mercury's magnetosphere-solar wind interaction for northward and southward interplanetary magnetic field: Hybrid simulation results, *Icarus*, *209*, 11–22, doi:10.1016/j.icarus.2010.01.008.

Wang, C. P., L. R. Lyons, J. M. Weygand, T. Nagai, and R. W. McEntire (2006), Equatorial distributions of the plasma sheet ions, their electric and magnetic drifts, and magnetic fields under different interplanetary magnetic field B_z conditions, *J. Geophys. Res.*, *111*, A04215, doi:10.1029/2005JA011545.

Winslow, R. M., C. L. Johnson, B. J. Anderson, H. Korth, J. A. Slavin, M. E. Purucker, and S. C. Solomon (2012), Observations of Mercury's northern cusp region with MESSENGER's Magnetometer, *Geophys. Res. Lett.*, *39*, L08112, doi:10.1029/2012GL051472.

Yagi, M., K. Seki, Y. Matsumoto, D. C. Delcourt, and F. Leblanc (2010), Formation of a sodium ring in Mercury's magnetosphere, *J. Geophys. Res.*, *115*, A10253, doi:10.1029/2009JA015226.

Zurbuchen, T. H., et al. (2011), MESSENGER observations of the spatial distribution of planetary ions near Mercury, *Science*, *333*, 1862–1865, doi:10.1126/science.1211302.